Rock Mechanics and Rock Engineering (2020) 53:3133–3147
https://doi.org/10.1007/s00603-020-02100-8

ORIGINAL PAPER

The Signature of Deformation Bands in Porous Sandstones

Huanran Wu[1] · Jidong Zhao[1] · Weijian Liang[1]

Received: 3 September 2019 / Accepted: 24 March 2020 / Published online: 13 April 2020

Abstract
Accurate identification and differentiation of various deformation bands in porous sandstone constitute a critical first step towards thorough understanding of these failure patterns. Two conventional ways prevail on band identification for sandstone, one based on a kinematic definition of shear offset (the ratio between shear and compaction displacement S/C) and the other according to a geometric inclination angle between band orientation and the principal stress direction. The two methods are not always consistent with each other, frequently leading to confusions or false identification of band patterns, especially when a deformation pattern is in transition. Employing an advanced multiscale modeling approach, we have reproduced a complete kinematic spectrum of deformation bands in porous sandstone. Enlightened by an exponential relation between $|\epsilon_v/\epsilon_q|$ and $|S/C|$ observed in the results, a new, accurate classifier, $B_i = \epsilon_v/\epsilon_q$, is proposed in this study, where ϵ_v and ϵ_q denote, respectively, the volumetric and deviatoric strains inside a band. The validity and robustness of B_i are examined with rigorous mechanical analyses in conjunction with insights drawn from multiscale modeling of localized deformation. Instead of decomposing the displacements, we further propose splitting the deformation gradient into four distinct kinematic components: (1) deviatoric compaction, (2) lateral extension, (3) simple shear, and (4) rigid rotation. As an end member of the kinematic spectrum, a pure dilation band (PDB) is found dominated by lateral extension without apparent compaction, shear, or rotation; a pure compaction band (PCB) is dominated by deviatoric compaction without apparent extension, shear, or rotation; a simple shear band (SSB) distinguishes itself from the previous two with the presence of substantial, proportional compaction, extension, shear, and rotation. As transitional patterns, shear-enhanced dilation band (SEDB), and shear-enhanced compaction band (SECB) are closer to pure volumetric deformation bands (PDB and PCB), while dilatant shear band (DSB) and compactive shear band (CSB) are more similar to simple shear band. In addition, B_i shows advantages in characterizing spatial variation and temporal transition of band patterns in complex boundary-value problems of sandstone.

Keywords Deformation band · Compaction band · Kinematic spectrum · Classification index · Porous sandstone · Multiscale modeling

1 Introduction

Porous sandstones are crucial hosts worldwide for hydrocarbons, water reservoirs, CO_2 sequestration and storage, as well as hazardous waste disposal (Holcomb et al. 2007; Olsson et al. 2002). Frequently observed in sandstones are narrow tabular zones with highly localized strains and small offsets called deformation bands (Aydin 1978; Fossen 2010). A complete kinematic spectrum range from pure dilation band (PDB), simple (isochoric) shear band (SSB), pure compaction band (PCB), and their hybrids with different relative magnitude of volumetric and shear deformations (Fossen et al. 2017). Their differences in physical nature may dictate their geological and engineering significance. Shear bands, for example, as a common band pattern with high shear deformation, have been observed during the failure of a rock specimen or around an underground excavation (Yang et al. 2012; Li et al. 2018; Francois et al. 2014; Pardoen et al. 2015). Compaction bands, on the other hand, represent a special, new class of deformation bands featuring intensive compaction without apparent shear deformation within the localized zone. They have been observed in both field outcrops and laboratory tests (Eichhubl et al. 2010; Townend et al. 2008; Liu et al. 2015). The formation of deformation bands around a borehole could affect

✉ Huanran Wu
hwuan@connect.ust.hk

[1] Hong Kong University of Science and Technology, Clearwater Bay, Kowloon, Hong Kong

its operation or even cause its failure (Haimson 2007; Lee et al. 2016). The presence of deformation bands may induce a significant heterogeneity in permeability among the porous host rocks and potentially alter the behavior of pore fluid flow, causing adverse consequences for relevant engineering applications (Fossen et al. 2007).

Accurate identification of a deformation band pattern out of all these types constitutes a critical first step for reconstructing its paleostress states, investigating its operative mechanisms, and examining its interplay with the fluid extraction/injection processes in sandstone. Geologists have commonly followed a kinematically based index, defined by the ratio of shear (band-parallel) displacement to compaction (band-perpendicular) displacement (*S*/*C*, Fig. 1) (Soliva et al. 2013; Fossen et al. 2017). Meanwhile, there have been extensive experimental studies investigating deformation bands formed in sandstones under various laboratory conditions (Bésuelle et al. 2000; Townend et al. 2008; Tembe et al. 2008; Baud et al. 2015). In these studies, a geometrically based band angle relative to the principal stress direction, in conjunction with volumetric deformation, has been widely adopted to classify the observed failures in experiments, e.g., dilatant shear bands (brittle faulting), compactive shear bands, high-angle shear bands, and compaction bands (Bésuelle 2001; Tembe et al. 2008; Baud et al. 2015). The band angle classification method has also been followed by theoretical and numerical modellers in studying deformation bands (Das et al. 2014; Wang et al. 2008).

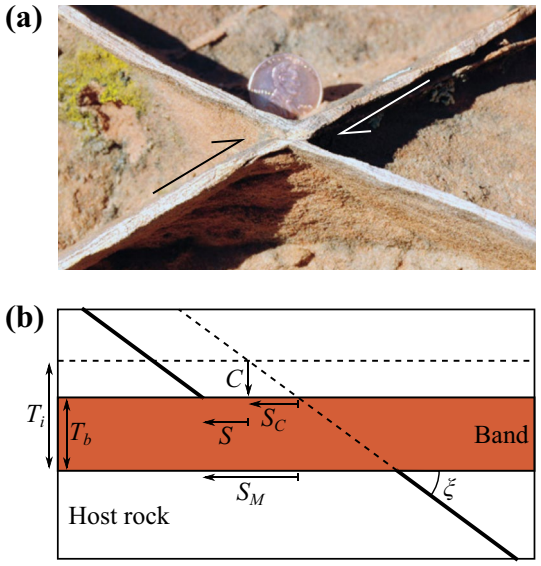

Fig. 1 Measurement of *S*/*C* in the field outcrops. **a** A demonstration of the shear offset in a shear-enhanced compaction band [after Fossen et al. (2011)]. **b** An illustration of compaction displacement ($C = T_b(\phi_i - \phi_b)/(1 - \phi_i)$, where ϕ_i and ϕ_b are the porosity of the host rock and the band, respectively) and shear displacement ($S = S_M - C/\tan\xi$) (Soliva et al. 2013)

Apparently, the above two methods on band classification are of different physical bases. There are cases where both *S*/*C* and band angle methods may offer vague, confusing or even false identifications of band patterns. Indeed, the detection of small shear offset is widely considered difficult for a shear-enhanced compaction band in the field, which may cause misinterpretations of some shear-enhanced compaction bands as pure compaction bands (Fossen et al. 2011). A sandstone may experience transition from one typical failure mode to another where both methods may experience difficulty to clearly differentiate. For example, experimental studies indicate that a sandstone tends to transit from brittle failure mode to ductile failure through a brittle–ductile transition with increased confining pressure (Tembe et al. 2008; Wong et al. 1997, 2001), whereby the angle of deformation bands with respect to the major principal stress (σ_1) may increase progressively (Baud et al. 2015; Bésuelle et al. 2000; Tembe et al. 2008). During the transition, mixed-mode failure patterns may co-exist, creating difficulties for accurate measurement of shear offset and/or band orientation. Importantly, notwithstanding their convenience for practical use, neither classification method could provide sufficiently robust, accurate insights into the fundamental physical mechanisms uniquely associated with each single type of deformation bands.

A new, physically based definition is proposed in this study to uniquely characterize and identify deformation band patterns in sandstone. For convenience of rigorous validation, we further employ a recently developed multiscale modeling approach (Guo and Zhao 2014, 2016b, a, c; Zhao and Guo 2015; Wu et al. 2017, 2018b; Nitka et al. 2011; Nguyen et al. 2014; Liu et al. 2016; Desrues et al. 2019) to reproduce different deformation bands in sandstone under various conditions. In this coupled FEM/DEM computational multiscale scheme, finite-element method (FEM) is adopted to solve the macroscopic boundary-value problems. A representative volume element (RVE), consisting of discrete particles, is attached at each Gauss point of the finite mesh to receive displacement gradient as microscopic boundary conditions and return stress information back through calculations using discrete element method (DEM). In this way, the phenomenological constitutive relationship in the conventional FEM is replaced by direct DEM computations to naturally take into account the discrete nature of granular materials. Detailed formulations of the multiscale modeling scheme are not provided here to avoid excessive repeat and defocusing of the study. Interested readers may refer to (Guo and Zhao 2014) and (Wu et al. 2018a) for details about this scheme. Based on the numerical results, we verify the accuracy and robustness of this new band index, and further discuss its potential as a better replacement over the conventional ways for future study of deformation and failures in sandstone.

2 A Complete Spectrum of Deformation Bands by Computational Multiscale Simulations

Existing studies on deformation bands have mainly been focused on the compaction side of the kinematic spectrum, since most deformation bands are between SSB and PCB (Fossen et al. 2017). However, experiments indicate the possibility of dilatant brittle failure of rocks under low confinement which may transit to PCB with the increase in confining pressure. Though relatively rare, PDBs have indeed been reportedly found in the field outcrop (Du Bernard et al. 2002). At the beginning of this study, a coupled FEM/DEM computational multiscale approach is first employed in attempting to reproduce a complete kinematic spectrum of deformation bands, including both dilatant and compactive types. The simulation results will serve as numerical bases in conjunction with the experimental and field data reported in the literature in guiding the ensuing theoretical discussion on deformation band classifier.

2.1 Biaxial Loading Tests

The simulations are performed on specimens of 50 mm × 80 mm (W × H). The domain is discretized into 12 × 20 eight-node quadratic quadrilateral elements, with two weak points being inserted at the center to trigger the deformation bands (Fig. 2). The failure of the specimen can be induced by either horizontal extension or vertical compression, while constant confining pressure is maintained during the loading process. For biaxial extension tests (Fig. 2a), a constant confining pressure σ_1 is exerted on the top and the bottom boundaries, and the lateral boundaries of the domain are assumed to be smooth, with a fixed left center. For biaxial compression tests (Fig. 2b), a constant confining pressure σ_0 is exerted on the lateral boundaries and both the top and bottom boundaries are assumed to be smooth, with a fixed bottom center. The axial strain (ϵ_a, ϵ_0 for extension tests and ϵ_1 for compression tests) is increased at a loading rate of 0.01% per step to induce failure. Following this scheme, the minor principal stress (σ_0) is along the x_0 axis and the major principal stress (σ_1) in the x_1 direction. The magnitude of confining pressure (σ_1 or σ_0) is varied to trigger different types of deformation bands under a wide range of principal stresses. While tests with positive principal stresses are common in both experiments and tectonic settings, tests with a

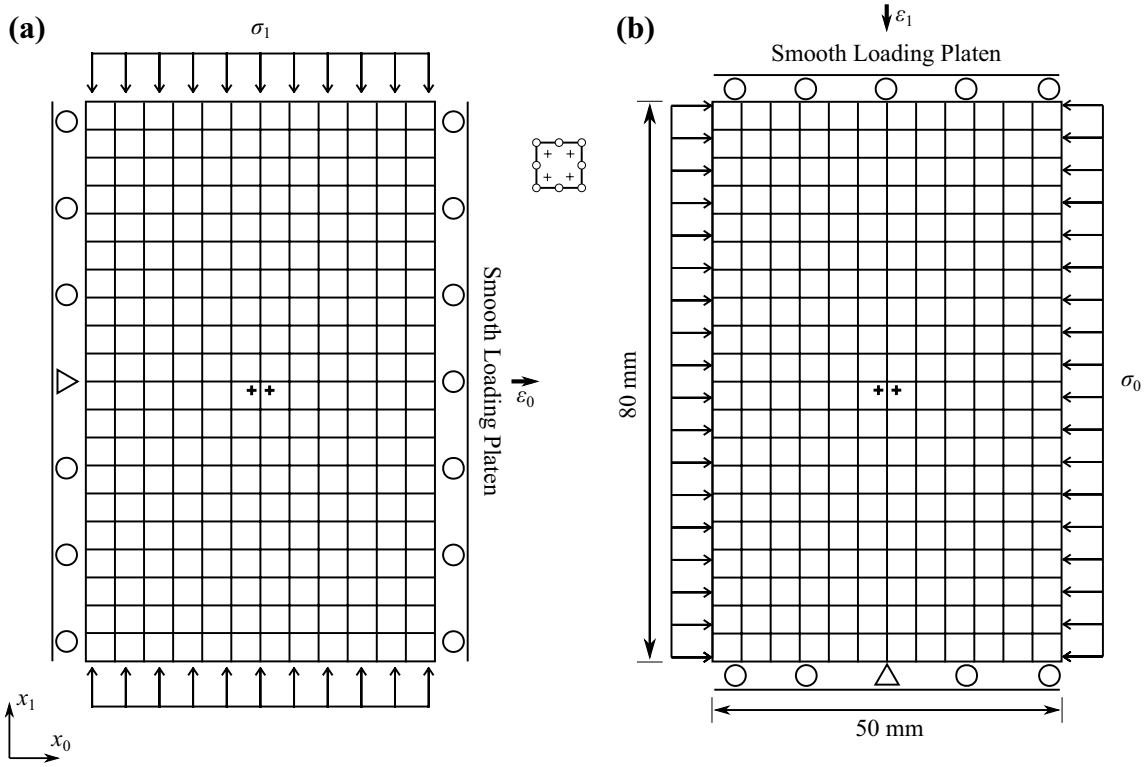

Fig. 2 FE discretization by eight-node quadratic quadrilateral elements with four Gauss integration points (reduced integration) and boundary conditions for **a** the biaxial extension tests and **b** biaxial compression tests, respectively. The black crosses in the center mark the two pre-inserted weak points of lower cohesion ($c = 5.44$ GPa) in each specimen

negative principal stress are rare in experiments, but, indeed, exist in extensional tectonic settings (Ramsey and Chester 2004; Soliva et al. 2016; Stoxreiter et al. 2019).

2.2 RVE for Porous Sandstones

Varied degree of grain crushing has been observed in shear bands in laboratory experiments on porous sandstones (Charalampidou et al. 2011; El Bied et al. 2002). As for compaction bands, particle crushing has been reported to be intense in laboratory experiments, but has been found significantly less severe in the field outcrops (Holcomb et al. 2007; Aydin and Ahmadov 2009). The focus of the present study is placed upon the characterization of a complete kinematic spectrum of deformation bands based on the relative magnitude of volumetric and shear deformations. Therefore, grain crushing will not be considered herein (Aydin et al. 2006). The reader is referred to (Fossen et al. 2007) for another classification scheme based on the dominant deformation mechanisms (e.g., granular flow, cataclasis, etc.). Indeed, shear bands in granular rocks have been investigated through DEM with unbreakable particles and bonded particle models (Cheung et al. 2013; Dinç and Scholtès 2018). Moreover, both shear and compaction bands have been reproduced with high-porosity RVEs without involving particle crushing (Wu et al. 2018a, 2019a). An RVE of similar structure (2D, porosity: 0.326, see Fig. 3) is employed in this study to represent the behavior of porous sandstones. The macropores in the RVE are considered to represent the macropores in porous sandstones presenting a shape and a size similar to that of grains (Charalampidou et al. 2014; Baud et al. 2015). The high-porosity structure is generated by removing some pre-inserted large particles and rattlers with less one contact in the RVE. Detailed preparation scheme could be found in (Wu et al. 2018a). An RVE with similar structure has been employed in (Wu et al. 2018b, 2019b).

The inter-particle contact model in the DEM comprises a linear force–displacement contact law, a Coulomb-type friction, and normal and tangential contact bonds. The normal (k_n) and tangential (k_t) contact stiffnesses are defined by two user-defined parameters E_c and ν_c according to $k_n = E_c r^*$ and $k_t = \nu_c k_n$, where $r^* = 2r_1 r_2/(r_1 + r_2)$, r_1 and r_2 are the radii of the two contacted particles (note that ν_c is not Poisson's ratio here). The contact bond is governed by a maximum tensile force ($F_n^{\max} = c \min(r_1, r_2)^2$) and a maximum tangential force ($F_t^{\max} = c \min(r_1, r_2)^2 + F_n \tan\phi$). If either of the thresholds is exceeded, the bond will be eliminated, leaving a pure frictional contact governed by the Coulomb's friction law (i.e., $F_t \le F_n \tan\phi$). Microparameters for DEM particles are summarized in Table 1. The particle density of 2650 kg/m^3 and the internal friction angle ϕ of 35° are common values in DEM simulations for sands and sandstones. The parameters for stiffness and cohesion (i.e., $E_c = 950$ GPa, $\nu_c = 1.0$, and $c = 6.8$ GPa) are calibrated, such that the modeled specimen yields a uniaxial compression strength (UCS) of 37.5 MPa. Though this study is not meant to simulate the behavior of a specific sandstone but rather trying to capture the general behavior of a wide class of sandstones, the calibrated UCS is close to the values (42 and 22 MPa) for two high-porosity Berea sandstones wherein compaction bands were observed (Haimson 2003).

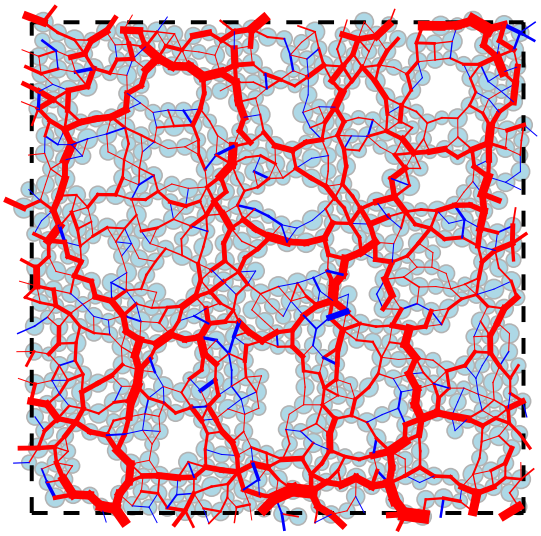

Fig. 3 Initial high-porosity RVE structure under isotropic confining pressure of 40 MPa (porosity: 0.326). The radii of the circular particles are linearly distributed from 0.2 to 0.3 mm. The red and blue lines illustrate the normal contact forces (red for compressive forces and blue for tensile forces) (color figure online)

2.3 Complete Spectrum of Deformation Bands

Figure 4 shows a selection of deformation bands reproduced in our multiscale simulations on the high-porosity RVE (shown in terms of contours of normalized debonding number (N), to quantify damage). From left to right, It is notable in the figure that the orientation of the band relative to the minor principal stress (σ_0) direction displays a continuous change from almost perpendicular in the uniaxial extension test (Fig. 4a) to parallel direction for the biaxial compression

Table 1 Microparameters for the discrete particles in the RVE

Parameter	Value
Particle radii r (mm)	0.2–0.3
Particle density ρ (kg/m^3)	2650
Interparticle friction angle ϕ (°)	35
E_c (GPa)	950
ν_c	1.0
Cohesion strength c (GPa)	6.8

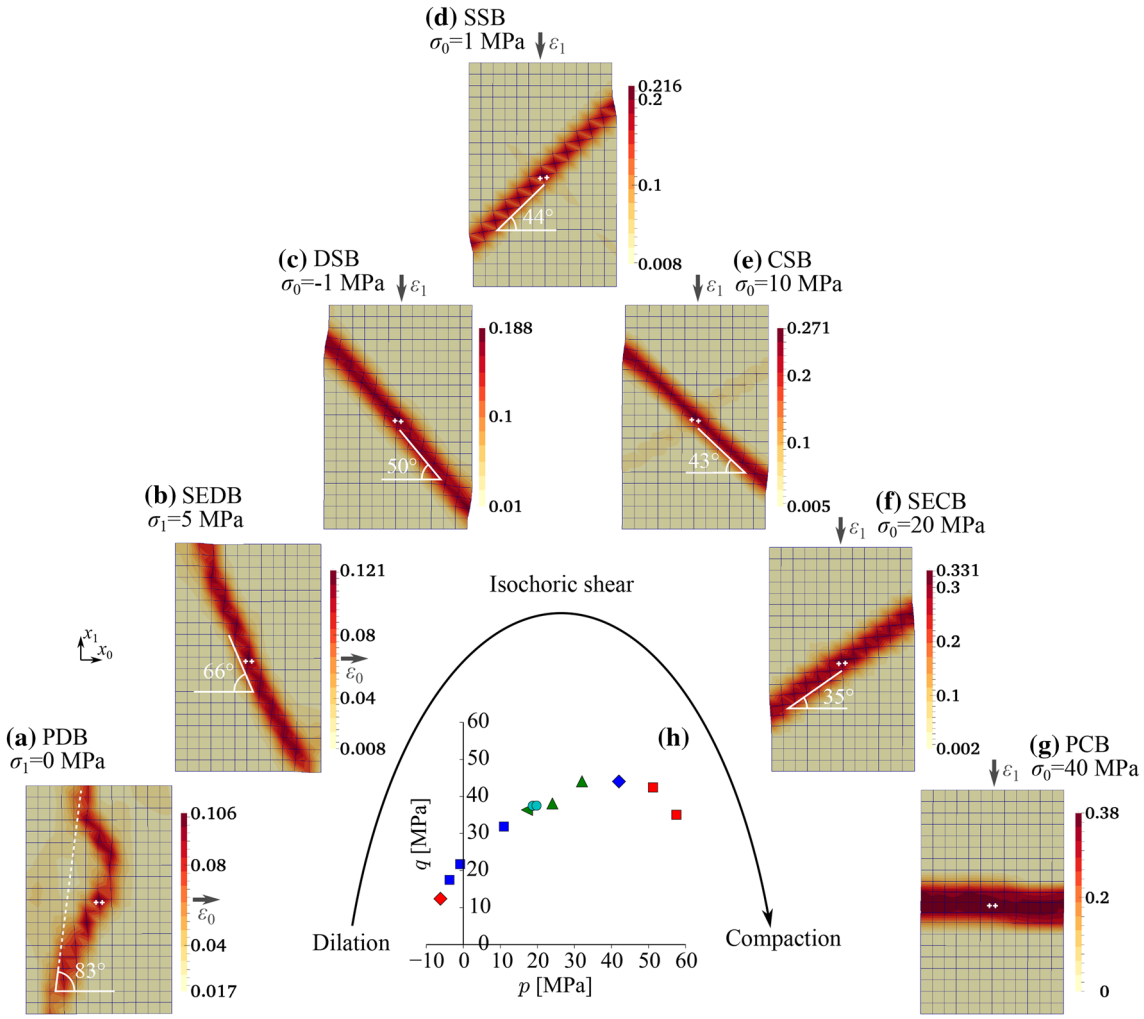

Fig. 4 The complete kinematic spectrum of deformation bands in multiscale simulations in terms of normalized debonding number (to quantify damage) (**a**–**g**). **h** Peak stress state for different tests in terms of differential stress (q) and mean stress (p), with different markers indicating the change of band pattern from pure dilation band (PDB), through shear-enhanced dilation band (SEDB), dilatant shear band (DSB), simple shear band (SSB), compactive shear band (CSB), and shear-enhanced compaction band (SECB), to pure compaction band (PCB) with the increase in p

test under $\sigma_0 = 40$ MPa (Fig. 4g). As the band perpendicular to σ_0 is recognized as PDB and the one parallel to σ_0 as PCB, the displayed bands cover a complete kinematic spectrum. Detailed classification will be discussed later. The peak stresses obtained in all the numerical simulations are plotted as differential stress (q) to mean stress (p) (Fig. 4h), with different markers indicating different types of deformation bands. It demonstrates clearly a continuous transition from PDB through SSB to PCB with increased p. This is a well-recognized phenomenon in laboratory experiments on sandstones (Fortin et al. 2006; Tembe et al. 2008).

The occurrence of different types of deformation bands may cause changes in porosity and permeability of sandstone in a distinctive manner. For instance, PDB has been reported to cause increase in porosity and permeability as compared to its host rock (Du Bernard et al. 2002), whereas PCB reduces the porosity and hence induces permeability drop up to three orders of magnitude (Aydin and Ahmadov 2009; Deng et al. 2015). Although a higher permeability has been reported in some dilatant shear bands (Han et al. 2016; Sun et al. 2013), a majority of shear bands show a reduction in permeability of up to six orders of magnitude (due to intense particle crushing) (Fossen and Bale 2007; Fossen et al. 2007; Ballas et al. 2014). Notwithstanding the wide variations (related to the grain-crushing intensity, mineral content, loading history, etc.), the changes in permeability caused by several typical deformation bands are summarised in the porosity–permeability space in Fig. 5. In plotting the figure, a modified version of the seminal Kozeny–Carman equation has been adopted in conjunction with our multiscale simulation results to consider the effects of porosity, grain size, and tortuosity as the dashed curves, together with

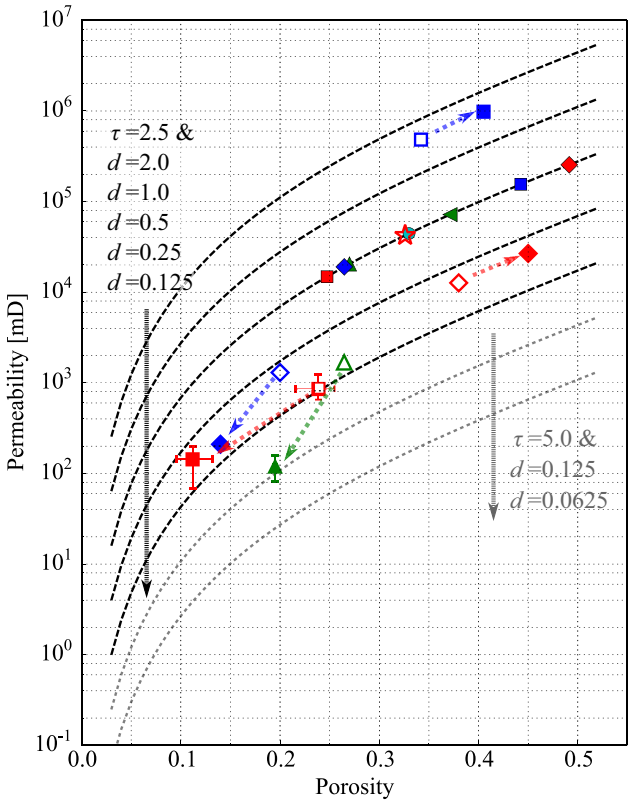

Fig. 5 Variations in permeability induced by the complete spectrum of deformation bands with open markers indicating their initial states and solid ones indicating their final states. See the meanings of different markers in Fig. 4. The variations in permeability caused by various deformation bands reported from the literature have been presented as pairs of open and solid markers connected by arrows (error bars to present the range if a set of data are available). Data for PCB (*Aztec*) are extracted from (Aydin and Ahmadov 2009), SECB (*Aztec*) from (Sun et al. 2011), CSB (*Chapus*) from (Ballas et al. 2014), DSB (*DEM–LBM modeling*) from (Sun et al. 2013), PDB (*McKinleyville*) is an estimation based on data from (Du Bernard et al. 2002), and Eq. 1 assuming $\tau = 2.5$

data reported in the literature (denoted by open and solid markers) (Mavko et al. 2009; Deng et al. 2015):

$$k = \frac{10^9}{72}\frac{n^3 d^2}{(1-n)^2\tau^2}, \tag{1}$$

where k is the permeability in mD, n is porosity, τ is tortuosity, and d is average particle size in mm. While the relatively larger reduction for CSB may be associated with a combined effect of grain crushing and a higher tortuosity, the changes for PCB, SECB, DSB, and PDB are governed by the variations in porosity. In plotting the curves in Fig. 5, we have taken two constant cases of τ, $\tau = 2.5$ and $\tau = 5.0$, to offer a crude estimation of the variations in permeability for the complete spectrum of deformation bands in Fig. 4a–g. Governed by the changes in porosity, a reduction in permeability

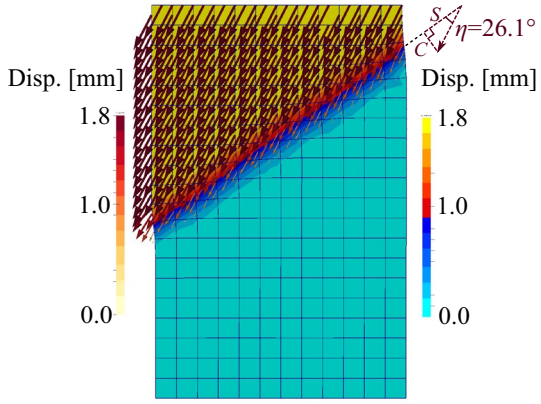

Fig. 6 Demonstration of $S/C = \cot\eta$ in multiscale simulations. The straight deformation band separates the displacement field within the specimen into a fixed lower part (in cyan) and a rigidly moved upper part (in yellow), and the gradually transitional band area (color figure online)

is observed for the compaction side and an increase is noted for the dilation side. The variations in contrast to the initial state are within one order of magnitude.

3 Classical and New Classifications of Deformation Bands

3.1 Conventional Classifications Based on Band Angle and *S*/*C*

Band angle appears to be a convenient and straight-forward choice for the classification of deformation bands. Indeed, in the complete kinematic spectrum of deformation bands, Fig. 4 confirms a continuous decrease in band angle from the almost vertical PDB to the horizontal PCB. However, the band-angle-based classification is not always reliable and/or feasible and sometimes may cause confusions, especially when a band is twisted, as will be demonstrated by examples presented in later sections.

Meanwhile, geologists have popularly employed a classification of deformation bands based on *S*/*C* where *S* and *C* denote, respectively, the shear displacement and compaction displacement measured in a band (see Fig. 1). Soliva et al. (2013) analyzed three sets of deformation bands in France and found that the mean value of *S*/*C* is around 25 for normal shear bands, around 10 for CSB and around 1 for SECB. Fossen et al. (2017) further summarized the *S*/*C* values for various band types in different outcrops around the world and suggested that CSB featured the highest *S*/*C* ratio ranging from 4 to larger than 100, while SECB showed moderate value smaller than 2 and PCB presented the smallest value close to 0.

In our multiscale simulations, S/C can be calculated directly from $S/C = \cot\eta$, where η is the angle between the displacement direction and the band direction (Fig. 6). For the case with a single straight deformation band, the angle η, the shear displacement S, and the compaction displacement C can be obtained readily. The obtained S and C for each case at four selected axial strain levels (0.5%, 1.0%, 1.5%, and 2.0%) are presented in Fig. 7a. Three selected field measurements are presented as well for reference. Since the maximum axial strain in the simulations is only 2.0%, the displacements (S and C) are much smaller than the field measurements. A zoomed view is hence presented as the inset. Notably, the data points for each case roughly form a straight line through the origin indicating an almost constant S/C. Although it may seem to be subjective, placing numeric bounds for S/C may help the classification. Figure 7a depicts various S/C in dashed lines and a schematic classification scheme is illustrated along the horizontal axis in Fig. 7d. The boundaries for the compaction side of the spectrum are based on the field data in conjunction with the multiscale results, and those for the dilation side are extended by regarding dilation bands and compaction bands equally as volumetric deformation bands (Aydin et al. 2006). It is clearly demonstrated that S/C is negative on the dilation side and positive on the compaction side. Meanwhile, an increase in $|S/C|$ is notable as the band pattern changes from pure volumetric deformation band (PDB and PCB) through shear-enhanced dilation/compaction band (SEDB and SECB) and dilatant/compactive shear band (DSB and CSB) to simple shear band (SSB).

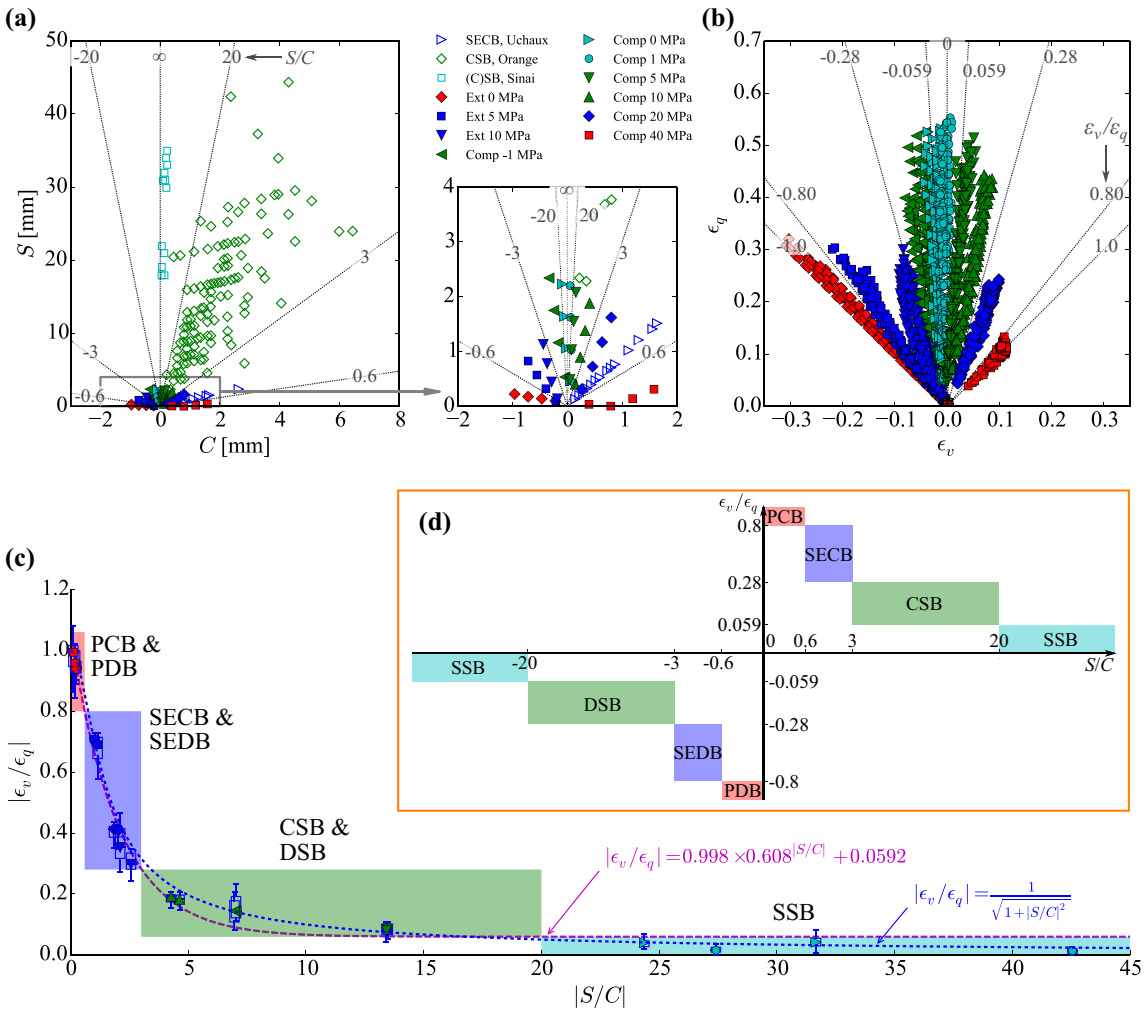

Fig. 7 **a** Shear displacement (S) to compaction displacement (C) for the multiscale simulations. Three sets of field measurement data (*SECB, Uchaux* from (Soliva et al. 2013), and *CSB, Orange* and *(C)SB, Sinai* from (Fossen et al. 2017)) are plotted as open markers for reference. The solid markers are simulation data (Ext for extension tests and Comp for compression tests). **b** Deviatoric strain (ϵ_q) vs. volumetric strain (ϵ_v) for the multiscale simulations. **c** The relation between $|\epsilon_v/\epsilon_q|$ and $|S/C|$. **d** The schematic diagram of the detailed classification scheme based on S/C and ϵ_v/ϵ_q (color figure online)

3.2 A Micromechanism-Based Index ϵ_v/ϵ_q

Despite its clarity, the classification based on *S*/*C* has not been commonly adopted in either experiments or numerical simulations. As suggested by Charalampidou et al. (2014), obtaining the local compaction and shear displacements is laborious and inaccurate, and it is especially so when the orientation of the band may vary. An apparent gap exists between theoretical and experimental studies and field observations on deformation bands in sandstone, which demands an alternative, better option on band classifications to reconcile the inconsistencies of the two communities. Strain decomposition into deviatoric strain (ϵ_q) and volumetric strain (ϵ_v) has been widely used in geomechanics to quantify the distortion and volume changes of geomaterials. The dominance of shearing in shear bands and significant volumetric change in compaction bands have been confirmed in both experiments and previous multiscale simulations (Charalampidou et al. 2011; Wu et al. 2018a). We, therefore, explore first the correlation between the ratio between deviatoric strain (ϵ_q) and volumetric strain (ϵ_v) and the deformation band patterns.

The deviatoric strain (ϵ_q) to volumetric strain (ϵ_v) of ten selected in-band RVEs for all our simulations is plotted in Fig. 7b. It is interesting to note that the data points for each case form a roughly straight line and the line turns steeper as the band change from pure volumetric deformation band to SSB. Expectedly, ϵ_v is negative for the dilation side and positive for the compaction side. Since the complete spectrum goes through SSB with $\epsilon_v \approx 0$, the dashed lines in the figure indicate different ϵ_v/ϵ_q whose value increases monotonically from PDB to PCB. The numeric boundaries for ϵ_v/ϵ_q are equivalent to those for *S*/*C*, which will be discussed in the next section. Detailed classification scheme based on ϵ_v/ϵ_q is presented along the vertical axis in Fig. 7d.

3.3 Correlation Between ϵ_v/ϵ_q and *S*/*C*

Given the similar observations in the microscale strains and the macroscale displacements, it is interesting to inspect the correlation between ϵ_v/ϵ_q and *S*/*C* in band differentiation. Figure 7c displays $|\epsilon_v/\epsilon_q|$ to $|S/C|$, assuming the same correlation for the compaction side and the dilation side. $|\epsilon_v/\epsilon_q|$ of the ten selected in-band RVEs obtained at the mature stage in each case ($\epsilon_a = 1.5\%$ and 2.0%) are shown as the boxplots with the markers indicating their median values. A clear exponential correlation between the two ratios is observed as the dashed magenta curve. The numeric boundaries for ϵ_v/ϵ_q in Fig. 7b and d are calculated based on this correlation and an assumed equivalence between the two classification schemes. An immediate advantage offered by the classification based on ϵ_v/ϵ_q is its continuous value for SSB rather than the sudden changes of *S*/*C* between $+\infty$ and $-\infty$ due to the alteration of tiny compaction displacement between positive and negative. A single straight deformation band developed in previous 2D cases leads to a straightforward calculation of *S*/*C*. However, this may not be the case for a curved band or multiple bands. In contrast, obtaining in-band ϵ_v/ϵ_q is convenient for numerical simulations, and poses no difficulty for modern experiments including the X-ray tomography and digital image correlation techniques (Andò et al. 2012; Charalampidou et al. 2011).

Meanwhile, it is widely regarded difficult, if not entirely impossible, to directly obtain ϵ_v and ϵ_q in the field given the lack of information on the reference configuration prior to the occurrence of deformation bands. The conventional classification based on *S*/*C* simplifies the deformation features inside deformation bands into fully decoupled one-dimensional normal strain (perpendicular to the band) and simple shear strain (parallel to the band) and, indeed, reflects the relative dominance of compaction and shear to some extent (Fossen et al. 2007, 2017; Soliva et al. 2013). Following the same simplification (neglecting lateral extension and rigid rotation, see the detailed analyses on microscale in-band deformation features in Sect. 4), one can obtain the deformation gradient as $\mathbf{F} = \begin{bmatrix} 1 & S/T_i \\ 0 & 1 - C/T_i \end{bmatrix}$, where T_i is the reference thickness of the deformation band (see Fig. 1b). The strain tensor can be derived as $\epsilon = \frac{1}{2}(\mathbf{F} + \mathbf{F}^T) - \mathbf{I} = \begin{bmatrix} 0 & S/2T_i \\ S/2T_i & -C/T_i \end{bmatrix}$, where $\mathbf{I}$ is the identity matrix. Taken compactive strain as positive, one can obtain the volumetric strain $\epsilon_v = C/T_i$ and deviatoric strain $\epsilon_q = \sqrt{C^2 + S^2}/T_i$. Hence, we can transform reliable field measurements of *S*/*C* into ϵ_v/ϵ_q following:

$$\epsilon_v/\epsilon_q = \frac{C}{\sqrt{C^2 + S^2}} = \frac{\pm 1}{\sqrt{1 + (S/C)^2}}, \tag{2}$$

where positive is for the compaction side and negative for the dilation side. This simplified correlation has been plotted in Fig. 7c as the blue dotted line. The good agreement between the measurements and the simplified correlation confirms its applicability for relatively simple cases displaying a single straight deformation band with clear passive markers (e.g., the one in Fig. 1a). Note the overprediction of this correlation from the measurements around the transition from shear-enhanced dilation/compaction band (SECB & SEDB) to dilatant/compactive shear band (CSB & DSB) with medium $|\epsilon_v/\epsilon_q|$ and $|S/C|$, due evidently to the complex coupling effects of deviatoric compaction, lateral extension, simple shear, and rigid rotation.

4 Microscale In-band Deformation Features

The new index ϵ_v/ϵ_q is a classifier based on the in-band deformation features. A visualization of those deformation features and quantitative comparison among different

deformation bands help to justify the use of this new index. To illuminate the distinct microscale deformation features inside various deformation bands, we decompose the deformation gradient **F** into three parts:

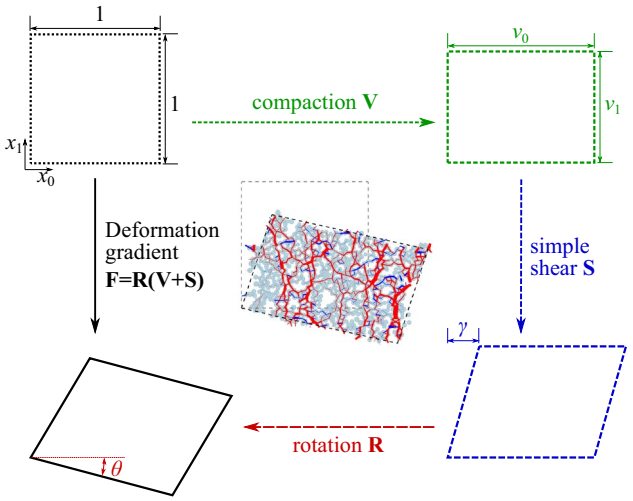

Fig. 8 Illustration of the deformation decomposition scheme. The RVE packing in the center demonstrates the microscale deformation from the original gray square to the final black parallelogram

$$\mathbf{F} = \mathbf{R}(\mathbf{V} + \mathbf{S}) \tag{3}$$

where, in a 2D setting, $\mathbf{R} = \begin{bmatrix} \cos\theta & -\sin\theta \\ \sin\theta & \cos\theta \end{bmatrix}$ is the rotation matrix, $\mathbf{V} = \begin{bmatrix} v_0 & 0 \\ 0 & v_1 \end{bmatrix}$ is the compaction part which may cause volume change, and $\mathbf{S} = \begin{bmatrix} 0 & \gamma \\ 0 & 0 \end{bmatrix}$ is the simple shear part without any volume change. The above expression is indeed a variation of the traditional polar decomposition where the deformation gradient is commonly decomposed into a rotation tensor and a symmetric stretch tensor. Figure 8 shows the schematic of the decomposition with visual illustration of the effect of each component. According to the figure, the microscale deformation features of a typical material point (or RVE in this study) can be characterized by (1) deviatoric compaction $(1 - v_1)$, (2) lateral extension $(v_0 - 1)$, (3) simple shear (γ), and (4) rigid rotation (θ).

To examine the microscale deformation features, ten typical in-band RVEs for each case in Fig. 4 are selected for analysis. Figure 9a and c show the statistical results for the dilation side and the compaction side of the kinematic spectrum, respectively. In the figures, the middle lines indicate the median values for each quantity surrounded by shaded lower and upper bounds according to the first and

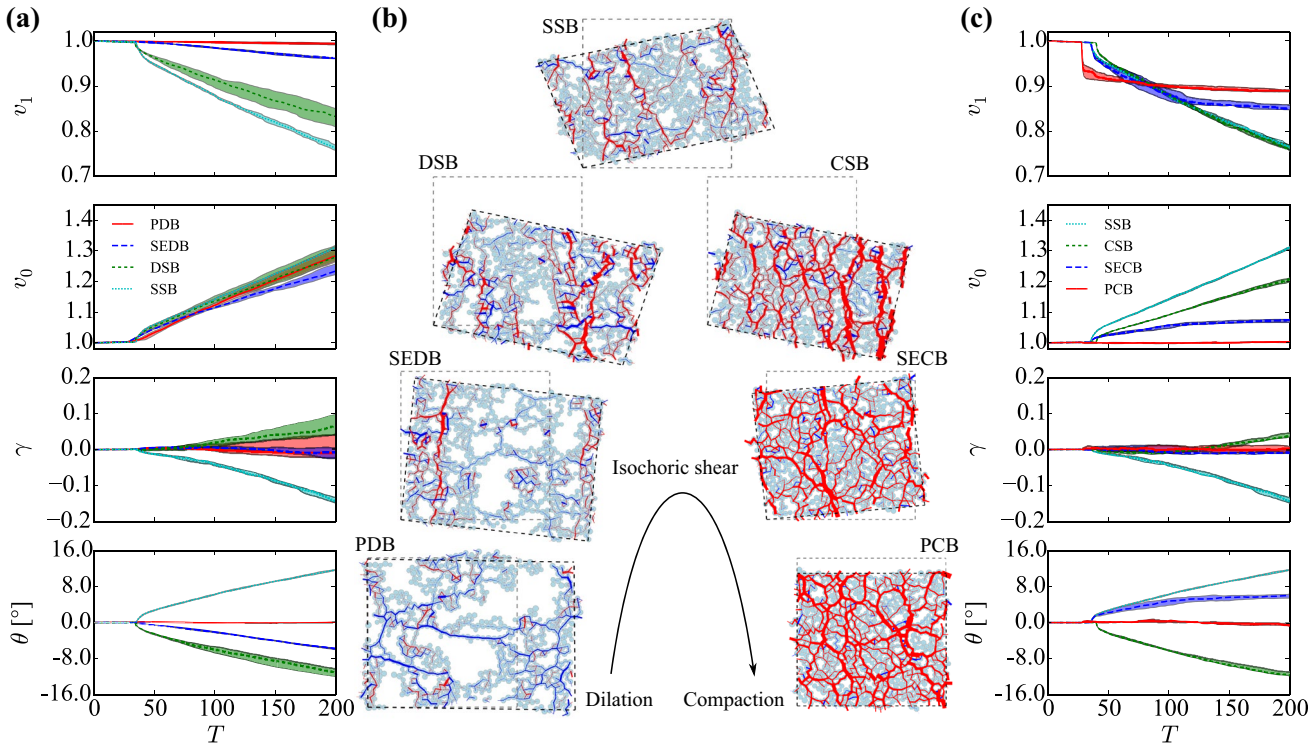

Fig. 9 Comparison of in-band deformation features. The evolution of deformation components with loading steps for **a** the dilation side and **c** the compaction side of the kinematic spectrum. **b** The typical in-band RVE structure at the final state when $\epsilon_a = 2.0\%$. The circles represent discrete particles and the short lines indicate the normal force between two contacted particles (red for compressive contacts and blue for tensile contacts) (color figure online)

third quartiles. The typical in-band RVE structure at the final stage are presented as Fig. 9b for illustration. Evidently, PDB is characterized by pure lateral extension with no apparent deviatoric compaction, shear, or rotation. In contrast, PCB features pure deviatoric compaction with almost no horizontal extension, shear, or rotation. On the other hand, SSB, another extreme case in the spectrum, presents substantial, proportional compaction, extension, shear, and rotation. As their hybrids, SEDB and SECB present features closer to pure volumetric deformation bands, while DSB and CSB display features more similar to SSB.

5 Using ϵ_v/ϵ_q for Band Identification

In the simulations shown in Fig. 4, a pair of weak points have been placed in the sample to trigger the straight deformation bands. In this idealized situation, the band angle and *S*/*C* are straightforward to determine. However, heterogeneity and randomness are inherent features of natural sandstone where deformation bands may frequently present in forms of curved, mixed, or vague patterns that are difficult to classify based on either band angle or *S*/*C*. It is demonstrated here that ϵ_v/ϵ_q, based on in-band deformation features, provides better, clear classifications in such complex situations on band identification.

5.1 ϵ_v/ϵ_q to Distinguish the Spatial Variation of Band Patterns

The sample with one pair of weak points producing a straight SECB in Fig. 4f is modified to include two pairs of weak points (shown as white crosses in Fig. 10b) as a new Case I. Under the same confining pressure σ_0 of 20 MPa, the final failure pattern in terms of normalized debonding number N is shown in Fig. 10b, showing to be a curved deformation band which could be approximately divided into three straight segments based on the band angle. The two blue ellipses indicate the bands with relatively gentle angle (Zone i and Zone iii), while the green ellipse refers to a segment of the bands with steep angle (Zone ii).

The evolution of ϵ_v/ϵ_q and four kinematic features (v_1, v_0, γ, and θ) of selected RVEs in Zone i and iii (blue ellipses) and Zone ii (the green ellipse) are plotted in Fig. 10a. Evidently, prior to the initiation of deformation bands, all four quantities in the three zones show no difference at all.

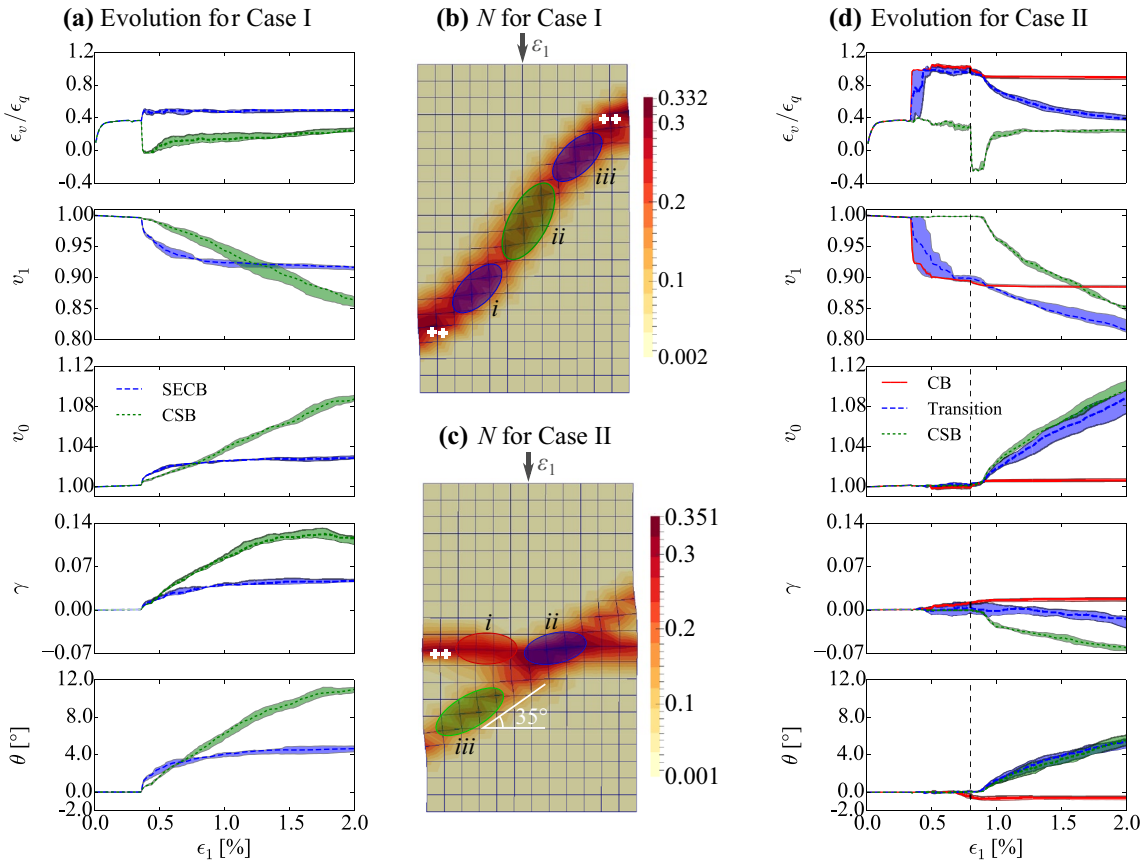

Fig. 10 Evolution of new band identifier ϵ_v/ϵ_q and the kinematic features v_1, v_0, γ and θ with ϵ_1 and contours of N to show the band patterns for (**a**, **b**) Case I and (**c**, **d**) Case II (color figure online)

$\epsilon_1 = 0.38\%$ marks the initiation of deformation bands for this cases and also a distinct bifurcation of ϵ_v/ϵ_q and other kinematic features for Zones i and iii with respect to Zone ii. In Zones i and iii with a gentle band angle, ϵ_v/ϵ_q shows a sudden jump of mild magnitude as the bands initiate, followed by a roughly constant value of around 0.5 throughout the rest of the development stage of the bands. The constant value of ϵ_v/ϵ_q is within the range of SECB. Indeed, the kinematic features of these two zones, in terms of v_1, v_0, and θ, further confirm with the same features of SECB, as shown in Fig. 9 very well. The slightly larger γ may have been caused by the influence of Zone ii. On the other hand, ϵ_v/ϵ_q of the steep band angle region (Zone ii) shows a relatively big sudden drop to almost 0 at the band initiation due to unloading and then gradually regain its value to a constant value of around 0.2, which is in the range of CSB. The evolutions of its linearly increased deviatoric compaction and lateral extension and relatively large shear and rotation all agree well with the kinematic features of CSB as discussed before. Consequently, the distinct developments of ϵ_v/ϵ_q and conformed kinematic features shown in Case I indicate absolutely different failure modes in the gentle and the steep bands. The gentle bands could be classified as SECB, while the steep zone is indeed a CSB. Since the band angle of Zone i (or iii) exhibits not significant difference than that in Zone ii, band angle classification may fail in this case. The *S*/*C* method fails to yield any clue in this case either.

5.2 ϵ_v/ϵ_q to Characterize the Temporal Transition of Band Patterns

While Case I has been designed to show the spatial variation of band patterns, the following example, Case II, is designed to show the temporal (or sequential, since the simulation has been quasi-static) transition of band patterns from one type to another during the loading process. Indeed, different deformation bands have been discovered at a same outcrop in the field (Aydin and Ahmadov 2009; Eichhubl et al. 2010). Key properties including material properties such as porosity and grain size and their spatial distribution can be controlling factors attributable to these band patterns (Schultz et al. 2010). Meanwhile, other factors, such as the change of stress states/conditions, constitute equally important factors that cannot be ignored. Fossen et al. (2011) suggested that CBs, SECBs, and CSBs observed at the same outcrop may have developed sequentially with the increase in mean stress. Charalampidou et al. (2017) demonstrated by experiments that CBs can be developed with increased confining pressure after the formation of SB at a relatively low confinement.

The sample in Case II is sheared at an initial confining pressure $\sigma_0 = 30$ MPa and then σ_0 is decreased to 10 MPa at $\epsilon_1 = 0.8\%$. With the change of confining pressure, complex band pattern transitions develop in Case II (which will be described in conjunction with the following analysis). The final failure pattern, shown in Fig. 10c, consists of a horizontal band and an inclined band. The evolutions of ϵ_v/ϵ_q in conjunction with the four kinematic parameters of typical RVEs from three typical zones indicated in Fig. 10c are shown in Fig. 10d. The dashed vertical lines in Fig. 10d mark the axial strain level at which σ_0 is decreased from 30 MPa to 10 MPa. When the specimen is loaded under $\sigma_0 = 30$ MPa, a horizontal CB is initiated from the pre-inserted weak points (shown as white crosses in Fig. 10c) at $\epsilon_1 = 0.36\%$. ϵ_v/ϵ_q of Zone i shows a sudden increase and then stays roughly constant at a value of around 1.0 until the decrease in σ_0. Its kinematic features agree well with those of CB as shown in Fig. 9, featuring a substantial deviatoric compaction with vanishingly small lateral extension, shear, or rotation. The inclined band starts to initiate soon after the decrease in σ_0. ϵ_v/ϵ_q of Zone iii shows a sudden drop to below 0 due to unloading, followed by a short flat stage and then a quick increase to a constant value of around 0.25, falling precisely into the range of CSB. Meanwhile, the almost proportionally increased deviatoric compaction, lateral extension, shear, and rigid rotation all agree well with the kinematic features of CSB, as shown in Fig. 9. It is interesting to examine the evolution of Zone ii which is the intersection of the initial CB and the ensuing CSB. ϵ_v/ϵ_q in Zone ii keeps almost constant during the development of CB stage and then decrease gradually to around 0.4 after the change of confining pressure. Clearly, Zone ii is initiated as a CB and then transits to a SECB when the confining pressure is decreased. Its kinematic features depict a rather consistent evolution, from CB to CSB. In the CSB stage, Zone ii shows almost identical v_0 and θ as Zone iii, while its decreasing rate of v_1 and increasing rate of γ are smaller than their counterparts for Zone iii due to its compaction at the CB stage.

The inclined band in Case II displays a band angle of $\beta = 35°$, which is equal to the value for SECB formed under $\sigma_0 = 20$ MPa, as shown in Fig. 4f. However, it is of CSB in nature as verified from the evolutions of ϵ_v/ϵ_q and kinematic features. This shows band angle along can be rather unreliable on band classification, while ϵ_v/ϵ_q can offer great advantages in this case. The gradual decrease in ϵ_v/ϵ_q for Zone ii from 1.0 to 0.4 clearly indicates the capability of using ϵ_v/ϵ_q to identify the sequential transition of band patterns during a loading process.

6 Conclusions

We have numerically modelled the complete kinematic spectrum of deformation bands in sandstone based on coupled FEM/DEM multiscale simulations. A new micromechanism-based classifier, $B_i = \epsilon_v/\epsilon_q$, has been proposed for

unified, robust classification of band patterns among full range of pure dilation band (PDB), shear-enhanced dilation band (SEDB), dilatant shear band (DSB), simple shear band (SSB), compactive shear band (CSB), shear-enhanced compaction band (SECB), and pure compaction band (PCB). The advantages offered by B_i on band identification were demonstrated by examples in comparison with the conventional classification methods. By decomposing the deformation gradient into four components: (1) deviatoric compaction $(1 - v_1)$, (2) lateral extension $(v_0 - 1)$, (3) simple shear (γ), and (4) rigid rotation (θ), we have further quantitatively verified the in-band deformation features associated with the proposed band classifier. Major findings in this study are summarized below.

1. The new index B_i can distinguish different deformation band patterns in both spatially variable and temporally evolving localisation conditions in sandstone when it is difficult to measure displacement decompositions for geological classification according to S/C or judging merely from band angles becomes highly unreliable.
2. An exponential correlation can be established between $|\epsilon_v/\epsilon_q|$ and $|S/C|$ to unify the existing data reported on deformation bands based on the geological classifier S/C, while the new index ϵ_v/ϵ_q offers clearly wider and continuous coverage of a complete spectrum of band ranges than the latter.
3. The study shows that, as three end members of the kinematic spectrum of deformation bands, (1) pure dilation band is characterized by pure lateral extension with no deviatoric compaction, shear, and rotation; (2) pure compaction band features pure deviatoric compaction with almost no lateral extension, shear, or rotation; (3) simple shear band exhibits most significant shear and rotation with substantial deviatoric compaction and lateral extension. Their hybrid (or transitional) patterns, including shear-enhanced dilation band and shear-enhanced compaction band, share more similarities to the pure volumetric deformation bands, whilst dilatant shear band and compactive shear band resemble more to simple shear band.

The validation of ϵ_v/ϵ_q as a micro-mechanically based kinematic classifier has been based on a correlation between $|\epsilon_v/\epsilon_q|$ and $|S/C|$. Its application in laboratory experiments is readily achievable with modern techniques on the measurement of strain field, such as particle image velocimetry (White et al. 2003) and digital image correlation (Andò et al. 2012; Charalampidou et al. 2014). Nevertheless, the numeric boundaries delineating the different types of deformation bands suggested in the study have been determined with the limited data of 2D simulations. Further validations of the new classifier and the recommended bounding values are certainly necessary by new data and observations from field, laboratory, and numerical simulations.

Acknowledgements The study has been financially supported by the National Natural Science Foundation of China under project 51679207 and the Research Grants Council of Hong Kong through GRF project 16210017. All figures were generated by the open-source data analysis toolkit (Python with the NumPy/SciPy and matplotlib packages, Paraview, and Inkscape). The software code used for modeling and generating the data in this study is based on the open-source parallel hierarchical multiscale modeling code FEM×DEM accessible via Yade (https://yade-dem.org/doc/FEMxDEM.html).

Compliance with ethical standards

Conflict of Interest The authors declare that they have no conflict of interest.

Appendix: Mesh-Dependency Analysis

The coupled FEM/DEM scheme in this study has been based on a non-regularized FEM formulation which may suffer mesh-dependency and make the post-localization results questionable. Advanced regularization techniques, e.g., Cosserat models and second gradient theory (Desrues et al. 2019; Rattez et al. 2018), are required to resolve this issue. On the other hand, the adoption of high-order elements with reasonable fine mesh has been found helpful to mitigate mesh-dependency (Guo and Zhao 2016b). Two more biaxial compression tests under $\sigma_0 = 10$ MPa have been conducted with different meshes (6×10 and 18×30) to analyze the mesh-dependency.

Figure 11a–c shows the final failure mode of different meshes at $\epsilon_1 = 2.0\%$ in terms of normalized debonding number. Despite the different band width and the different in-band damage intensities, the failure mode is similar with the same band angle. The stress–strain relations for the three cases are presented in Fig. 11d. Due to the pre-inserted weak points to trigger the localization, the coarse mesh (6×10) produces the smallest stress peak and the fine mesh (18×30) produces the largest. It is worth noting that the difference in peak stress between the medium-fine mesh (12×20) and the fine mesh is less than 2%. The post-peak behaviors of these two cases are almost the same, as well. Typical in-band RVEs are selected to calculate the evolution of the proposed index ϵ_v/ϵ_q as presented in Fig. 11e. The in-band RVEs in the medium-fine case and the fine case present almost the same evolution of ϵ_v/ϵ_q. It is worth noting that ϵ_v/ϵ_q for the coarse mesh tend to converge to the same value despite the difference as the localization occurs due to the stronger effect of the weak points. The results presented in Fig. 11 prove that the adoption of a reasonable fine mesh (12×20 in this study) mitigates the pathological mesh-dependency and justify the post-peak analyses conducted in this study.

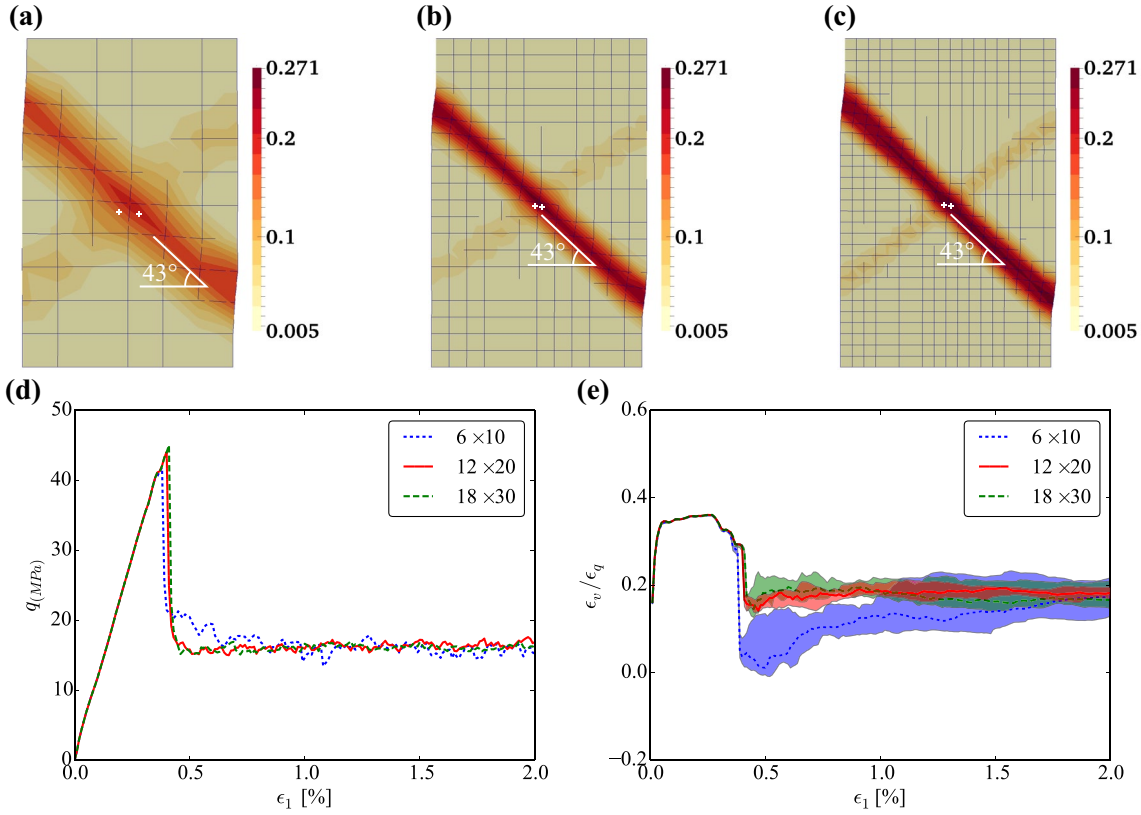

Fig. 11 Mesh-dependency analysis for the FEM/DEM multiscale modeling. **a**–**c** Failure mode at the final state in terms of normalized debonding number with two white dots marking the pre-inserted weak points. **d** The evolution of differential stress ($\sigma_1 - \sigma_0$) with axial strain. **e** The evolution of ϵ_v/ϵ_q with axial strain

References

Andò E, Hall SA, Viggiani G, Desrues J, Bésuelle P (2012) Grain-scale experimental investigation of localised deformation in sand: a discrete particle tracking approach. Acta Geotech 7(1):1–13. https://doi.org/10.1007/s11440-011-0151-6

Aydin A (1978) Small faults formed as deformation bands in sandstone. Pure Appl Geophys PAGEOPH111 116(4–5):913–930. https://doi.org/10.1007/BF00876546

Aydin A, Ahmadov R (2009) Bed-parallel compaction bands in aeolian sandstone: their identification, characterization and implications. Tectonophysics 479(3–4):277–284. https://doi.org/10.1016/j.tecto.2009.08.033

Aydin A, Borja RI, Eichhubl P (2006) Geological and mathematical framework for failure modes in granular rock. J Struct Geol 28(1):83–98. https://doi.org/10.1016/j.jsg.2005.07.008

Ballas G, Soliva R, Benedicto A, Sizun JP (2014) Control of tectonic setting and large-scale faults on the basin-scale distribution of deformation bands in porous sandstone (Provence, France). Mar Pet Geol 55:142–159. https://doi.org/10.1016/j.marpetgeo.2013.12.020

Baud P, Reuschlé T, Ji Y, Cheung CSN, Wong TF (2015) Mechanical compaction and strain localization in Bleurswiller sandstone. J Geophys Res Solid Earth 120(9):6501–6522. https://doi.org/10.1002/2015JB012192

Bésuelle P (2001) Compacting and dilating shear bands in porous rock: theoretical and experimental conditions. J Geophys Res 106(B7):13435–13442. https://doi.org/10.1029/2001JB900011

Bésuelle P, Desrues J, Raynaud S (2000) Experimental characterisation of the localisation phenomenon inside a Vosges sandstone in a triaxial cell. Int J Rock Mech Min Sci 37(8):1223–1237. https://doi.org/10.1016/S1365-1609(00)00057-5

Charalampidou EM, Stanchits S, Dresen G (2017) Compaction bands in a porous sandstone sample with pre-induced shear bands. In: Bifurcation and Degradation of Geomaterials with Engineering Applications, Springer, Cham, Springer Series in Geomechanics and Geoengineering, pp 391–398. https://doi.org/10.1007/978-3-319-56397-8_48

Charalampidou EM, Hall SA, Stanchits S, Lewis H, Viggiani G (2011) Characterization of shear and compaction bands in a porous sandstone deformed under triaxial compression. Tectonophysics 503(1–2):8–17. https://doi.org/10.1016/j.tecto.2010.09.032

Charalampidou EM, Hall SA, Stanchits S, Viggiani G, Lewis H (2014) Shear-enhanced compaction band identification at the laboratory scale using acoustic and full-field methods. Int J Rock Mech Min Sci 67:240–252. https://doi.org/10.1016/j.ijrmms.2013.05.006

Cheung LYG, O'Sullivan C, Coop MR (2013) Discrete element method simulations of analogue reservoir sandstones. Int J Rock Mech Min Sci 63:93–103. https://doi.org/10.1016/j.ijrmms.2013.07.002

Das A, Tengattini A, Nguyen GD, Viggiani G, Hall SA, Einav I (2014) A thermomechanical constitutive model for cemented granular materials with quantifiable internal variables. Part II—validation and localization analysis. J Mech Phys Solids 70(1):382–405. https://doi.org/10.1016/j.jmps.2014.05.022

Deng S, Zuo L, Aydin A, Dvorkin J, Mukerji T (2015) Permeability characterization of natural compaction bands using core flooding

experiments and three-dimensional image-based analysis: Comparing and contrasting the results from two different methods. AAPG Bull 99(01):27–49. https://doi.org/10.1306/07071413211
Desrues J, Argilaga A, Caillerie D, Combe G, Nguyen TK, Richefeu V, Pont SD (2019) From discrete to continuum modelling of boundary value problems in geomechanics: An integrated FEM-DEM approach. Int J Numer Anal Meth Geomech 43(5):919–955. https://doi.org/10.1002/nag.2914
Dinç Ö, Scholtès L (2018) Discrete analysis of damage and shear banding in argillaceous rocks. Rock Mech Rock Eng 51(5):1521–1538. https://doi.org/10.1007/s00603-017-1397-6
Du Bernard X, Eichhubl P, Aydin A (2002) Dilation bands: a new form of localized failure in granular media. Geophys Res Lett 29:24. https://doi.org/10.1029/2002GL015966
Eichhubl P, Hooker JN, Laubach SE (2010) Pure and shear-enhanced compaction bands in Aztec Sandstone. J Struct Geol 32(12):1873–1886. https://doi.org/10.1016/j.jsg.2010.02.004
El Bied A, Sulem J, Martineau F (2002) Microstructure of shear zones in Fontainebleau sandstone. Int J Rock Mech Min Sci 39(7):917–932. https://doi.org/10.1016/S1365-1609(02)00068-0
Fortin J, Stanchits S, Dresen G, Guéguen Y (2006) Acoustic emission and velocities associated with the formation of compaction bands in sandstone. J Geophys Res 111:B10203. https://doi.org/10.1029/2005JB003854
Fossen H (2010) Structural geology. Cambridge University Press, New York
Fossen H, Bale A (2007) Deformation bands and their influence on fluid flow. AAPG Bull 91(12):1685–1700. https://doi.org/10.1306/07300706146
Fossen H, Schultz R, Shipton Z, Mair K (2007) Deformation bands in sandstone: a review. J Geol Soc 164(4):1–15. https://doi.org/10.1144/0016-76492006-036
Fossen H, Schultz RA, Torabi A (2011) Conditions and implications for compaction band formation in the Navajo Sandstone, Utah. J Struct Geol 33(10):1477–1490. https://doi.org/10.1016/j.jsg.2011.08.001
Fossen H, Soliva R, Ballas G, Trzaskos B, Cavalcante C, Schultz RA (2017) A review of deformation bands in reservoir sandstones: geometries, mechanisms and distribution. Geol Soc Lond Spec Publ 459:9–33. https://doi.org/10.1144/SP459.4
Francois B, Labiouse V, Dizier A, Marinelli F, Charlier R, Collin FFF (2014) Hollow cylinder tests on boom clay: modelling of strain localization in the anisotropic excavation damaged zone. Rock Mech Rock Eng 47(1):71–86. https://doi.org/10.1007/s00603-012-0348-5
Guo N, Zhao J (2014) A coupled FEM/DEM approach for hierarchical multiscale modelling of granular media. Int J Numer Meth Eng 99(11):789–818. https://doi.org/10.1002/nme.4702
Guo N, Zhao J (2016a) 3D multiscale modeling of strain localization in granular media. Comput Geotech 80:360–372. https://doi.org/10.1016/j.compgeo.2016.01.020
Guo N, Zhao J (2016b) Multiscale insights into classical geomechanics problems. Int J Numer Anal Meth Geomech 40(3):367–390. https://doi.org/10.1002/nag.2406
Guo N, Zhao J (2016c) Parallel hierarchical multiscale modelling of hydro-mechanical problems for saturated granular soils. Comput Methods Appl Mech Eng 305(9):768–785. https://doi.org/10.1016/j.cma.2016.03.004
Haimson BC (2003) Borehole breakouts in berea sandstone reveal a new fracture mechanism. Pure Appl Geophys 160:813–831. https://doi.org/10.1007/PL00012567
Haimson BC (2007) Micromechanisms of borehole instability leading to breakouts in rocks. Int J Rock Mech Min Sci 44(2):157–173. https://doi.org/10.1016/j.ijrmms.2006.06.002
Han B, Xie SY, Shao JF (2016) Experimental investigation on mechanical behavior and permeability evolution of a porous limestone under compression. Rock Mech Rock Eng 49(9):3425–3435. https://doi.org/10.1007/s00603-016-1000-6
Holcomb D, Rudnicki JW, Issen KA, Sternlof K (2007) Compaction localization in the Earth and the laboratory: state of the research and research directions. Acta Geotech 2(1):1–15. https://doi.org/10.1007/s11440-007-0027-y
Lee H, Moon T, Haimson BC (2016) Borehole breakouts induced in arkosic sandstones and a discrete element analysis. Rock Mech Rock Eng 49(4):1369–1388. https://doi.org/10.1007/s00603-015-0812-0
Li XF, Zhang QB, Li HB, Zhao J (2018) Grain-based discrete element method (GB-DEM) modelling of multi-scale fracturing in rocks under dynamic loading. Rock Mech Rock Eng 51(12):3785–3817. https://doi.org/10.1007/s00603-018-1566-2
Liu C, Pollard DD, Gu K, Shi B (2015) Mechanism of formation of wiggly compaction bands in porous sandstone: 2. Numerical simulation using discrete element method. J Geophys Res Solid Earth 120(12):8153–8168. https://doi.org/10.1002/2015JB012374
Liu Y, Sun W, Yuan Z, Fish J (2016) A nonlocal multiscale discrete-continuum model for predicting mechanical behavior of granular materials. Int J Numer Meth Eng 106(2):129–160. https://doi.org/10.1002/nme.5139
Mavko G, Mukerji T, Dvorkin J (2009) The rock physics handbook: tools for seismic analysis of porous media, 2nd edn. Cambridge University Press, New York. https://doi.org/10.1017/CBO9781107415324.004
Nguyen TTK, Combe G, Caillerie D, Desrues J (2014) FEM x DEM modelling of cohesive granular materials: numerical homogenisation and multi-scale simulation. Acta Geophys 62(3):1109–1126. https://doi.org/10.2478/s11600-013-00
Nitka M, Combe G, Dascalu C, Desrues J (2011) Two-scale modeling of granular materials: a DEM-FEM approach. Granular Matter 13(3):277–281. https://doi.org/10.1007/s10035-011-0255-6
Olsson WA, Holcomb DJ, Rudnicki JW (2002) Compaction localization in porous sandstone: implications for reservoir mechanics. Oil Gas Sci Technol 57(5):591–599. https://doi.org/10.2516/ogst:2002040
Pardoen B, Seyedi DM, Collin F (2015) Shear banding modelling in cross-anisotropic rocks. Int J Solids Struct 72:63–87. https://doi.org/10.1016/j.ijsolstr.2015.07.012
Ramsey JM, Chester FM (2004) Hybrid fracture and the transition from extension fracture to shear fracture. Nature 428(6978):63. https://doi.org/10.1038/nature02333
Rattez H, Stefanou I, Sulem J, Veveakis M, Poulet T (2018) Numerical analysis of strain localization in rocks with thermo-hydro-mechanical couplings using cosserat continuum. Rock Mech Rock Eng 51(10):3295–3311. https://doi.org/10.1007/s00603-018-1529-7
Schultz RA, Okubo CH, Fossen H (2010) Porosity and grain size controls on compaction band formation in Jurassic Navajo sandstone. Geophys Res Lett 37(22):1–5. https://doi.org/10.1029/2010GL044909
Soliva R, Schultz RA, Ballas G, Taboada A, Wibberley C, Saillet E, Benedicto A (2013) A model of strain localization in porous sandstone as a function of tectonic setting, burial and material properties; new insight from Provence (southern France). J Struct Geol 49:50–63. https://doi.org/10.1016/j.jsg.2012.11.011
Soliva R, Ballas G, Fossen H, Philit S (2016) Tectonic regime controls clustering of deformation bands in porous sandstone. Geology 44(6):423–426. https://doi.org/10.1130/G37585.1
Stoxreiter T, Gehwolf P, Galler R (2019) Alternative approaches for the determination of unconfined rock deformation and strength properties. Rock Mech Rock Eng. https://doi.org/10.1007/s00603-019-01908-3
Sun W, Andrade JE, Rudnicki JW, Eichhubl P (2011) Connecting microstructural attributes and permeability from 3D tomographic images of in situ shear-enhanced compaction bands using

multiscale computations. Geophys Res Lett 38:L10301. https://doi.org/10.1029/2011GL047683

Sun WC, Kuhn MR, Rudnicki JW (2013) A multiscale DEM-LBM analysis on permeability evolutions inside a dilatant shear band. Acta Geotech 8(5):465–480. https://doi.org/10.1007/s11440-013-0210-2

Tembe S, Baud P, Wong TF (2008) Stress conditions for the propagation of discrete compaction bands in porous sandstone. J Geophys Res 113:B09409. https://doi.org/10.1029/2007JB005439

Townend E, Thompson BD, Benson PM, Meredith PG, Baud P, Young RP (2008) Imaging compaction band propagation in Diemelstadt sandstone using acoustic emission locations. Geophys Res Lett 35(15):1–5. https://doi.org/10.1029/2008GL034723

Wang B, Chen Y, Wong TF (2008) A discrete element model for the development of compaction localization in granular rock. J Geophys Res 113:B03202. https://doi.org/10.1029/2006JB004501

White DJ, Take WA, Bolton M (2003) Soil deformation measurement using particle image velocimetry (PIV) and photogrammetry. Géotechnique 53(7):619–631. https://doi.org/10.1680/geot.2003.53.7.619

Wong TF, David C, Zhu W (1997) The transition from brittle faulting to cataclastic flow in porous sandstones: mechanical deformation. J Geophys Res 102(B2):3009–3025. https://doi.org/10.1029/96JB03281

Wong TF, Baud P, Klein E (2001) Localized failure modes in a compactant porous rock. Geophys Res Lett 28(13):2521–2524. https://doi.org/10.1029/2001GL012960

Wu H, Guo N, Zhao J (2018a) Multiscale modeling and analysis of compaction bands in high-porosity sandstones. Acta Geotech 13(3):575–599. https://doi.org/10.1007/s11440-017-0560-2

Wu H, Zhao J, Guo N (2018b) Multiscale insights into borehole instabilities in high-porosity sandstones. J Geophys Res Solid Earth 123(5):3450–3473. https://doi.org/10.1029/2017JB015366

Wu H, Zhao J, Guo N (2019b) Multiscale modeling of compaction bands in saturated high-porosity sandstones. Eng Geol 261:105282. https://doi.org/10.1016/j.enggeo.2019.105282

Wu H, Guo N, Zhao J (2017) Borehole instabilities in granular rocks revisited: a multiscale perspective. In: Papamichos E, Papanastasiou P, Pasternak E, Dyskin A (eds) Bifurcation and degradation of geomaterials with engineering applications, Springer, Cham, Springer Series in Geomechanics and Geoengineering, pp 433–439. https://doi.org/10.1007/978-3-319-56397-8_54

Wu H, Papazoglou A, Viggiani G, Dano C, Zhao J (2019a) Compaction bands in Tuffeau de Maastricht: insights from X-ray tomography and multiscale modeling. Acta Geotechnica. https://doi.org/10.1007/s11440-019-00904-9

Yang SQ, Jing HW, Wang SY (2012) Experimental investigation on the strength, deformability, failure behavior and acoustic emission locations of red sandstone under triaxial compression. Rock Mech Rock Eng 45(4):583–606. https://doi.org/10.1007/s00603-011-0208-8

Zhao J, Guo N (2015) The interplay between anisotropy and strain localisation in granular soils: a multiscale insight. Géotechnique 65(8):642–656. https://doi.org/10.1680/geot.14.P.184